Journal of Power Sources 490 (2021) 229523

Contents lists available at ScienceDirect

Journal of Power Sources

journal homepage: www.elsevier.com/locate/jpowsour

Pulse resistance based online temperature estimation for lithium-ion cells

S. Ludwig *, I. Zilberman, M.F. Horsche, T. Wohlers, A. Jossen

Technical University of Munich (TUM), Institute for Electrical Energy Storage Technology (EES), Arcisstrasse 21, 80333 Munich, Germany

ARTICLE INFO

Keywords:
Temperature estimation
Cell resistance
Battery management system
State estimation
Lithium-ion battery

ABSTRACT

Knowing the temperature distribution within a battery pack is vital, because of the impact on capacity loss, power degradation and safety. Temperature measurements are usually realized with temperature sensors attached to a limited number of cells throughout the battery pack, leaving the majority of cells in larger battery systems unattended. This work presents a novel sensorless method for determining the temperature of a cell by exploiting the relation of the cell's overpotential and temperature exemplary using a 18650 nickel-rich/silicon–graphite cell, although the method is basically applicable to any cell. Current changes in the battery load are utilized as pulse excitation for the calculation of a direct-current resistance $R_{DC,\Delta t}$ determined after a certain time Δt. Reference pulses at 10/20/30/40 °C are recorded to investigate the influence of state-of-charge and pulse rise/fall-time, as well as the pulse-current amplitude and direction on $R_{DC,\Delta t}$. The analysis of the reference pulses shows that a Δt in the 10 ms to 100 ms regime has the greatest sensitivity to temperature and the least dependence on other parameters. The method is finally validated using a 6s1p-module with an externally constant temperature gradient applied to the serial connection, showing an average estimation error smaller than 1 K for each cell.

1. Introduction

Monitoring the temperature of a lithium-ion battery (LIB) is a crucial task of a battery management system (BMS). The temperature not only influences the performance of the battery [1], but also the aging behavior [2–4] and safety [5,6]. In general, the temperatures of cells within a battery pack differ during operation [7,8], simply caused by the spatial location of the cells, which poses a challenging task for homogeneous cooling/heating of each cell [9,10]. The resulting temperature inhomogeneity within the battery pack may lead to safety issues and inhomogeneous aging [11,12]. Thermal simulations of the battery pack are capable of detecting systematic design flaws causing the inhomogeneous temperature distribution within a battery pack [13,14]. Nevertheless, simulations cannot take all events into account, such as deviations during pack assembly and intrinsic cell parameter variations. Also a shift of the pack temperature distribution during operation, for instance induced by cell aging, is difficult to model. Therefore, monitoring the temperature of each cell in the battery pack is of high interest for a BMS. Since a battery system can be composed of several hundred up to thousands of cells [15], monitoring each cell poses a difficult task. Increased wiring effort, hardware and BMS costs are the consequence, if temperature sensors are used [16]. Moreover, external sensors barely indicate the internal cell temperature and cover a limited area on the surface of the cell [17]. Electrochemical impedance spectroscopy (EIS) is proposed in several studies to partially overcome these challenges [16–23]. By utilizing the relation of a cell's temperature and certain features within the impedance spectrum, the temperature can be estimated without the use of an external temperature sensor. Using these EIS-based methods does not increase the wiring effort, since the existing connections for voltage monitoring can be utilized, but there is still the additional effort and cost for the hardware performing the sinusoidal excitation. Wang et al. [24] recently developed an approach using the instant current changes and the corresponding voltage response in the time domain as input for a wavelet transformation to calculate the cell impedance. With the transformed result they build on the findings of the EIS-based temperature estimation methods and use the impedance's phase at 10 Hz to estimate the temperature. Using pulses in the time domain is also used for estimating other critical battery states. For instance, Mathew et al. [25] have already shown that using only sharp current pulses for direct resistance estimation can be utilized for state-of-health (SOH) estimation. Their approach significantly reduces the required computational complexity compared to model-based solutions. With the pulse-based approach in the time domain the need for additional hardware for EIS measurements is eliminated. Load changes, which naturally occur during the operation of battery powered devices, such as acceleration or braking of an electric vehicle (EV), can be used as an excitation. Nevertheless, it is not ensured that the load changes

* Corresponding author.
E-mail address: sebastian.ludwig@tum.de (S. Ludwig).

https://doi.org/10.1016/j.jpowsour.2021.229523
Received 17 September 2020; Received in revised form 24 November 2020; Accepted 13 January 2021
Available online 1 February 2021

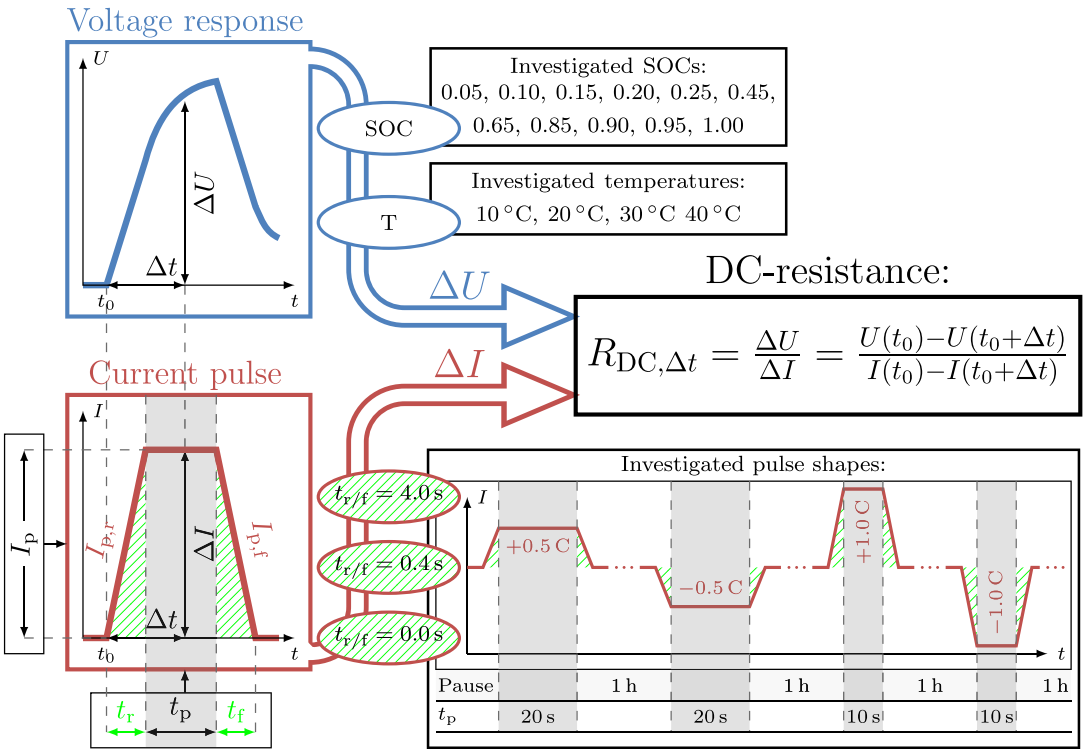

Fig. 1. Investigated SOCs, temperatures and pulse parameters.

in an application are perfectly pulse shaped. Therefore, this study has the goals to (i) find the criteria the pulses have to meet to be suitable for temperature estimation and (ii) develop a sensorless temperature estimation method in the time domain. The method only requires the generally monitored parameters, current and voltage, to calculate a direct current (DC) resistance $R_{DC,\Delta t} = \frac{\Delta U}{\Delta I}$ for a certain resistance-calculation-period Δt after a current change (pulse). The focus lies on a simple time domain based approach without the need for additional excitation hardware or a complex transformation from the time domain to the frequency domain, which is online applicable in a BMS.

The work is structured as follows. In the first step, different load changes, including rectangular and non-rectangular pulses, are experimentally evaluated at different temperatures and state-of-charges (SOCs). The relation of the resistance $R_{DC,\Delta t}$ and temperature is analyzed in terms of resistance-calculation-period Δt, the pulse parameters and the SOC. In the next step, the results of the analysis are incorporated in the parametrization of a temperature estimation function $T_{est} = f(R_{DC,\Delta t})$ and the search for the optimal resistance-calculation-period. Finally, the online applicability of the method is validated with a representative battery module of six serial connected cells.

2. Experimental

This chapter describes the investigated cell and the conducted experiments for the pulse parameter analysis and the method validation.

2.1. Investigated cell

The developed method aims at applications with changing load currents, such as EVs. The trend for EVs points to batteries with higher energy density and capacity. Nickel-rich lithium-ion cells are a recent chemistry to fulfill this demand, although they show a poor interfacial stability [26]. Silicon as an anode material or as an additive to a conventional graphite anode is also a recent development [27,28]. For this reason, a commercial nickel-rich NMC/SiC high-energy 18650 lithium-ion cell (INR18650-MJ1) from LG Chem with a nominal capacity of 3.5 Ah is the objective of the study. For a detailed chemistry description of this cell the authors refer to [12,29–31].

Table 1
Parameter overview with expectation (μ) and standard deviation (σ) of the cells used for the pulse parameter analysis at 25 °C. The capacity C_{act} was measured according to the manufacturer's standard CC discharge procedure with $I_{CC} = -0.2$ C from 4.2 V to 2.5 V followed by a CV stage with a cut-off current of $I_{CV} > -50$ mA. The resistance was determined at 50 % SOC with a discharge current pulse of 1.0 C. According to Sturm et al. [29] the composition of the active material of the cathode amounts to 82 % nickel, 6.3 % manganese and 11.7 % cobalt. The proportion of silicon in the anode amounts to 3.5 wt%.

Parameter	Cell			μ	σ
	C_1	C_2	C_3		
C_{act} / A h	3.389	3.421	3.407	3.406	0.016
$R_{DC,10s}$ / mΩ	45.3	44.2	45.0	44.7	0.569

2.2. Pulse experiment

The three selected cells for the pulse parameter analysis are listed in Table 1. Besides the temperature, several pulse parameters influence the voltage response, and thereby the resistive behavior of a cell. To investigate the influence of the pulse parameters and the temperature, an experiment with different pulses was conducted. Fig. 1 depicts the investigated influence factors on the DC-resistance $R_{DC,\Delta t}$. The influence of SOC and temperature on the voltage response was investigated by performing current pulses at eleven SOC steps and for four temperatures. To cover a large variety of possible load changes in an application, the shape of the current pulses was altered according to the pattern in Fig. 1. The pattern varied the pulse amplitude I_p, current direction and pulse duration t_p, and was performed at each SOC and temperature point. To investigate the influence of (non)-rectangular pulses, the pulse pattern was repeated for three different rise/fall-times $t_{r/f}$. The rise/fall-time refers to the individual pulse edges. To distinguish DC-resistances calculated on the rising edge and the falling edge of the pulse, the corresponding pulses are named $I_{p,r}$ for rising and $I_{p,f}$ for falling edges.

The details of the test sequence for the pulse parameter experiment are documented in Table 2. The sequence started with a 3 h pause to

Table 2
Test procedure for generating pulses with different parameters. Steps #1–3 were measured with a BaSyTec CTS. Steps #4–18 were measured with a BioLogic VMP3 with 5 A Booster. Temperatures were set with a Binder KT 115 climatic chamber with a maximal temperature fluctuation of ±0.1 K.

#	Step	Parameter	Termination
for T_{exp} = 10 /20 /30 /40 °C			
1	Pause	T = 25 °C	t > 3 h
2	Charge (CC)	I = +0.5 C	U > 4.2 V
3	Charge (CV)	U = 4.2 V	I < +50 mA
4	Pause	$T = T_{exp}$	t > 3 h
for SOC_{exp} = 0.95/0.90/0.85/0.65/0.45/0.25/0.20/0.15/0.10/0.05			
for $t_{r/f}$[a] = 0.0 /0.4 /4.0 s			
5	Charge pulse	I_p = +0.5 C, $t_{r/f}$	t_p > 20 s
6	Pause		t > 1 h
7	Discharge pulse	I_p = −0.5 C, $t_{r/f}$	t_p > 20 s
8	Pause		t > 1 h
9	Charge pulse	I_p = +1.0 C, $t_{r/f}$	t_p > 10 s
10	Pause		t > 1 h
11	Discharge pulse	I_p = −1.0 C, $t_{r/f}$	t_p > 10 s
12	Pause		t > 1 h
end			
13	Discharge (CC)	I = −0.2 C	SOC = SOC_{exp}
14	Pause		$\frac{\Delta U}{\Delta t}$ < 5 mV h^{-1}
end			
15	Discharge (CC)	I = −0.2 C	U < 2.5 V
16	Discharge (CV)	U = 2.5 V	I > −50 mA
end			

[a]Although the test device's minimal rise/fall-time for current changes is 40 µs, the "instant" current changes are denoted with $t_{r/f}$ = 0.0 s.

acclimatize the cells to the reference temperature of 25 °C. The cell was then fully charged by a constant-current (CC) charge according to the manufacturer's specifications followed by a constant-voltage (CV) phase. A period of 3 h of acclimatization at the corresponding experiment temperature T_{exp} is followed by a sequence of four pulses charging/discharging the cells according to Step #5 to #12. The selected pulse duration avoided larger SOC or temperature changes and the absolute charge-throughput of the pulses was equal. The pause of 1 h in between the pulses resulted in a voltage drift of less than ±2 mV h^{-1} before the subsequent pulse, which is sufficient enough to assume that the relaxation processes are almost completed and the pulses start from an equilibrated state. The sequence of four pulses from Step #5 to #12 was repeated for three different pulse rise/fall-times $t_{r/f}$ = 0.0 s, 0.4 s and 4.0 s. Subsequently, the SOC was adjusted according to Step #13. Since the voltage relaxation after Step #13 differs with temperature and SOC and may affect the result of the pulses [32,33], the following pause in Step #14 ended after the cell voltage change per hour was less than 5 mV h^{-1}. The pause was followed by the pulse pattern for the next SOC. Since the charge transfer resistance and diffusion resistance increases at the periphery of the SOC range [34,35], finer SOC steps were used towards the limits.

2.3. Validation experiment

To validate the temperature estimation method, a 6s1p-module of the same cell type was used. However, the cells of the module were not the same as the ones for the pulse parameter analysis. There were two reasons for this: (i) only three cells were used in the pulse parameter analysis and six were needed for the validation experiment; (ii) by using six different cells for the validation experiment the transferability of the method within the same cell type is demonstrated. The initial parameters of the six module cells (C_4 to C_9) are listed in Table 3. The module setup is shown in Fig. 2a and ensured different temperatures for each cell in the module but minimized a possible temperature gradient within the cylindrical cells [36]. Thereby, the comparison of the estimated temperature and the external reference temperature sensor

Table 3
Parameter overview with expectation (μ) and standard deviation (σ) of the cells used for the validation experiment at 25 °C. The cells were the same as in [12]. The capacity C_{act} was measured according to the manufacturer's standard CC discharge procedure with I_{CC} = −0.2 C from 4.2 V to 2.5 V followed by a CV stage with a cut-off current of I_{CV} > −50 mA. The resistance was measured at 50 % SOC with a discharge current of 1.0 C.

Parameter	Cell						μ	σ
	C_4	C_5	C_6	C_7	C_8	C_9		
C_{act}/Ah	3.461	3.469	3.461	3.47	3.462	3.463	3.464	0.004
$R_{DC,10s}$/mΩ	42.3	42.7	42.3	43.0	42.4	42.0	42.45	0.3507

was not distorted by cell internal temperature deviations. To achieve this, the cells of the module were wrapped in high thermal conductivity foil and enclosed in copper blocks to ensure thermal contact via heat conduction. The copper blocks with the embedded cell were screwed to a common copper rail with a Peltier element at each end of the rail. To ensure a minimal thermal transfer resistance between the copper rail and block, the contact area was lubricated with thermal grease. By setting the Peltier elements to different temperatures, a temperature gradient ΔT developed over the module. For more information about the module setup and cells, the authors refer to [12].

The validation scenario applied the current-profiles of 14 concatenated drive cycles of the 149 drive cycles presented by Campestrini et al. [37] to the 6s1p-module. With the variety of drive cycles, the method was tested for all kinds of EV application scenarios. Fig. 2b shows the resulting module current for the 14 drive cycles. While applying the drive cycles, a temperature gradient of ΔT = 5 °C from 25 °C to 30 °C was enforced on the module. Fig. 2c shows the sensor-offset corrected cell temperatures during the drive cycles. The offset calibration for all temperature sensors was performed at 25 °C. All six cells kept an almost constant temperature during the drive cycles with a maximal average deviation of ±0.086 K from the mean cell temperature.

3. Results and discussion

The first part of this chapter discusses the influence of temperature, SOC and the pulse parameters on the $R_{DC,\Delta t}$ by analyzing the results from the pulse experiment of Section 2.2. Subsequently, a temperature estimation method is proposed and benchmarked against the experimental pulse data. Lastly, the results of the estimation method are presented and validated with the module and driving profiles depicted in Fig. 2.

3.1. Parameter influence

The goal of this section is to narrow down the resistance-calculation-period Δt, in which the estimation method is the most resilient against any parameter variation.

Fig. 3 is utilized to interpret all investigated parameters (temperature, SOC and pulse shape) from the pulse experiment in Section 2.2. Each row of Fig. 3 depicts the influence on $R_{DC,\Delta t}$ for a specific pulse parameter and Δt over the SOC for all four experimental temperatures. The three investigated cells from Table 1 feature an almost equal curve shape, only differing in an resistance offset between the curves of the individual cells. For this reason, the curves depicted in Section 2.2 represent the average $R_{DC,\Delta t}$ of the three cells from Table 1 for a specific pulse parameter and Δt. The averaged DC-resistance values are scaled, allowing an easier comparison between the different time scales.

3.1.1. Temperature and SOC influence

This section focuses on the general temperature and SOC sensitivity of Fig. 3. The temperature has a major influence on the properties and processes of a lithium-ion cell. Be it the ionic/electronic conductivity of a cell's materials [38–40] or the electrochemical processes within the

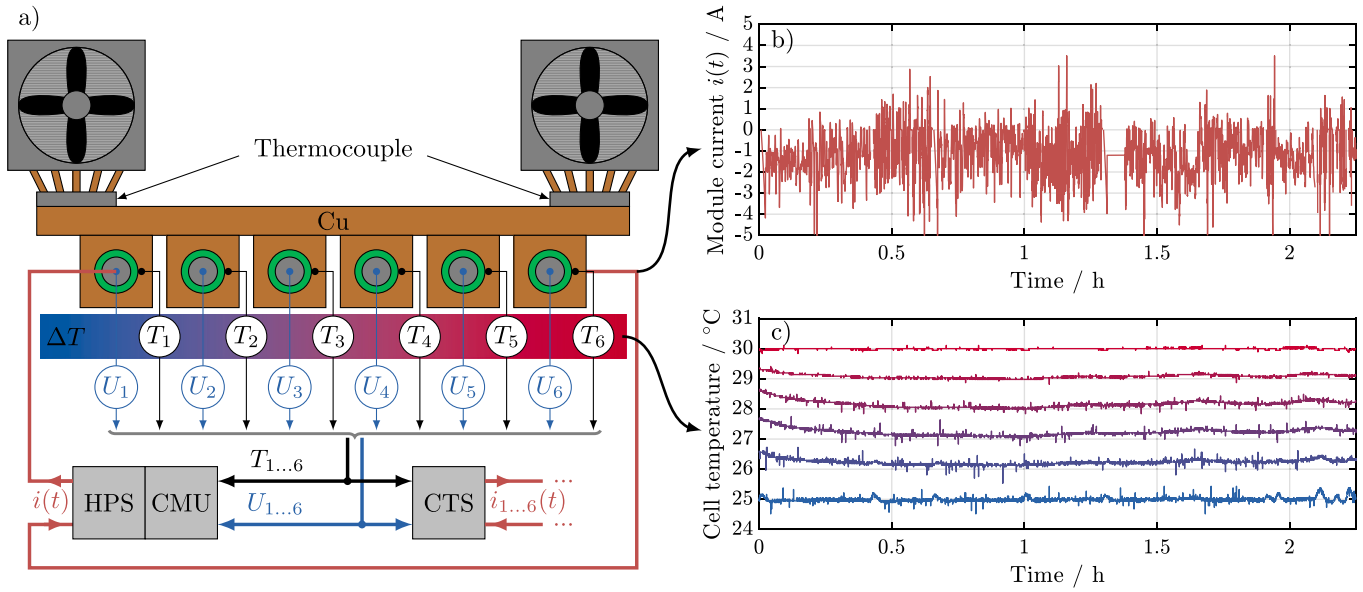

Fig. 2. Overview of the test setup for the 6s1p-module used for method validation (a) [12]. On the module level, a High-Power-System (HPS) was used to drive the module current $i(t)$. The temperature as well as the cell voltage was monitored with a Cell-Measurement-Unit (CMU). For cell level cycling and monitoring, each cell was connected to a Cell-Testing-System (CTS). To control the temperature gradient and measure the cell temperatures, PT100 temperature sensors were used. The temperature sensors for the cells were integrated in the copper blocks and mounted on the surface of each cell. Six clipboards connected the positive and negative tabs of each cell with gold contact pins in a 4-wire connection to a configuration plug, allowing measurements on the cell level as well as module level. BaSyTec measurement equipment accuracy as follows. HPS: precision of 0.05 %; CMU voltage measurement: resolution of 0.2 mV and accuracy of 2.5 mV; CMU temperature measurement: precision of 1 °C and resolution of <0.1 °C; CTS: accuracy of ±0.3 mV and ±0.5 µA in the smallest range for the voltage and current measurement. Applied module current $i(t)$ scaled to the limits of the cell (maximal charge current of 3.5 A) and the HPS (maximal current 5 A) (b), and corresponding cell temperatures T_1 to T_6 (c).

cell [41,42], all are affected by temperature and ultimately affect the $R_{DC,\Delta t}$. Depending on the resistance-calculation-period Δt, the voltage response ΔU is influenced by different processes, represented by three resistance-calculation-periods in Fig. 3a to Fig. 3f. The resistance-calculation-periods in Fig. 3a to Fig. 3f were selected according to the time scales for dynamic processes in lithium-ion batteries according to [42–44].

In Fig. 3a and Fig. 3d the resistance-calculation-period is set to 1 ms representing the shortest time scale, still allowing a reasonable sampling rate for a BMS. In this time domain, the major contribution to the DC-resistance comes from the ohmic losses of the cell [42,43]. The temperature behavior of the ohmic part is caused by the limited electronic conductivity of the current collectors, the electrodes, the electrolyte ionic conductivity and the conduction properties of their interfaces [45,46]. Except for the current collectors, all other materials show an increasing conductivity with increasing temperature. However, taking the overall high electronic conductivity of the current collectors into account, the contribution to the potential drop ΔU and the electronic conductivity change over temperature is negligibly small [42,47]. The temperature behavior of the anode's materials of the investigated cell, graphite [48,49] and silicon [50], has a minor effect on the $R_{DC,\Delta t}$, because both materials show a minor conductivity increase with increasing temperature compared to the other materials. The cathode of the investigated cell is made of nickel-rich NMC, which has a relatively low ionic/electronic conductivity with high Arrhenius-like temperature dependence [39,40]. Therefore, the cathode is most likely one of the main contributors to the temperature behavior of the cell's ohmic resistance. The other main contributor to the ohmic resistance with major dependence on temperature is the electrolyte, also with an Arrhenius-like behavior [38,42,51,52]. Since Δt = 1 ms does not only include the instant voltage response related to the sole ohmic losses of a cell, the solid electrolyte interface (SEI) and the charge transfer reaction also contribute to the $R_{DC,\ 1\ ms}$. Both, the SEI and the charge transfer reaction, are temperature dependent and increase in impedance with decreasing temperatures [17,21,35,41,42,52–54]. Besides the temperature influence, the dependence on SOC is apparent, especially at the periphery of the SOC range.

By increasing Δt to 10 ms in Fig. 3b and Fig. 3e, the contribution of the charge transfer reaction at both electrodes increases and its SOC dependence becomes even more apparent. In general, the charge transfer resistance can be described with an Arrhenius-like exponential dependency on temperature [42,52,55]. As a result, the distance between the curves of the different temperatures in Fig. 3b and Fig. 3e is more distinct compared to Fig. 3a and Fig. 3c, and the sensitivity of the DC-resistance for temperature changes is increased.

Fig. 3c and Fig. 3f depict the DC-resistance for Δt = 1000 ms. In this time domain the charge transfer reactions are completely included in the impedance with a partial contribution of the diffusion-driven processes. At the SOC extremes and lower temperatures, the charge transfer reaction has a dominant contribution to the resistance of the cell. Here, the electrodes are almost fully lithiated/delithiated and the intercalation/deintercalation is aggravated. Additionally, the increased resistance at lower temperatures is related to the slower diffusion of the lithium-ions within the electrodes [1,23,56,57].

Looking at the temperature and SOC behavior of the DC-resistance in all three representative time domains of Fig. 3a to Fig. 3f, the following two facts can be concluded:

1. The temperature behavior of the DC-resistance shows a non-linear behavior. It is assumed to be mainly influenced by the Arrhenius-like dependence of the relevant processes and materials in all investigated time domains.
2. The DC-resistance is SOC-dependent in all investigated time domains.

Compared to the other two time domains, a spread for the different pulse shape parameters, especially in the lower SOC region below 20 %, stands out for Δt = 1000 ms in Fig. 3c and Fig. 3f. A detailed investigation on this resistance spread and on the general pulse parameter influence in the different time domains is done in the next section.

3.1.2. Pulse shape influence

As depicted in Fig. 1, the current pulse shape was altered by changing several pulse parameters in the pulse experiment of Section 2.2

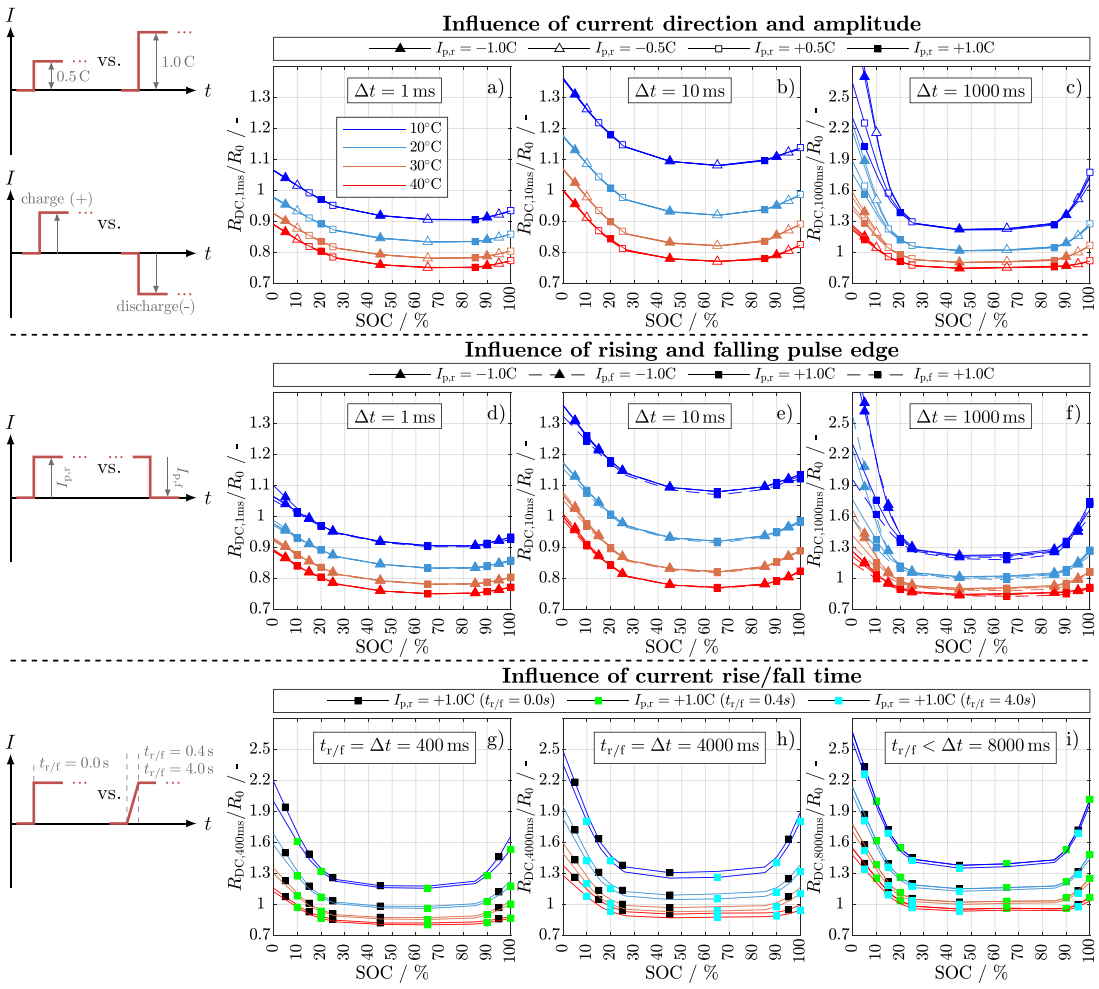

Fig. 3. Influence of the pulse parameters current amplitude/direction (a–c), excitation/idle pulses (d–f) and pulse rise/fall-time (g–i) on $R_{DC,\Delta t}$ for different Δt. $\Delta t = 1$ ms for (a,d), $\Delta t = 10$ ms for (b,e), $\Delta t = 1000$ ms for (c,f), $\Delta t = t_{r/f} = 400$ ms for (g), $\Delta t = t_{r/f} = 4000$ ms for (h) and $\Delta t = 8000$ ms for (i). All values are scaled to $R_0 = 40$ mΩ, which is the maximal cell impedance at 1 kHz, 23 °C and 100 % SOC according to the manufacturer's specifications. For the sake of clarity not all SOC markers for each curve are depicted.

to investigate the influence on the DC-resistance and to find the least parameter dependent time domain for Δt.

The first regarded parameters are the pulse current direction and the pulse amplitude. The first row, Fig. 3a to Fig. 3c, depicts the influence of the pulse current direction and the pulse amplitude at different Δt. Only rising pulses $I_{p,r}$ are included. There is no noteworthy difference between the $R_{DC,\Delta t}$ evident for short Δt (1 ms and 10 ms) in Fig. 3a and Fig. 3b. For longer Δt, such as in Fig. 3c, the resistance values increase, especially in the SOC regime below 20 % and temperatures of 20 °C and less. A possible explanation, also reported by [34] and [42], is the increased charge transfer and diffusion polarization. Besides the resistance increase, two additional effects are visible in Fig. 3c that can be explained with the Butler–Volmer equation [58,59]. The first one is the non-linearity of the voltage–current relation. With increasing current density the corresponding slope of activation overpotential decreases, which causes a smaller resistance for the pulses with a current of ±1.0 C compared to ±0.5 C. The second effect is the current direction dependency of the resistance values. The cathode approaches its lithiated state and the anode its delithiated state for the SOC regime below 20 %. In this case, the intercalation in the cathode active material, respectively the deintercalation out of the anode active material (discharge pulse), gets less favorable, while the reversed process (charge pulse) gets more favorable. Since the reaction rates of the electrochemical process decrease with temperature, the effect increases for lower temperatures. [42,60,61]

As a result, the resistance values of different temperatures start to overlap with increasing Δt, which makes the $R_{DC,\Delta t}$ in this time domain impractical for temperature estimation. The same effect with inverted pulse direction evolves for the SOC regime over 90 %. Since the electrodes are not fully utilized because of the limited stability of the electrolyte above 4.2 V [62] and the increased potential for lithium plating at a higher SOC during charging, the resistance increase and spread is less distinct. In terms of temperature estimation for the investigated cell, this means that the resistance-calculation-period Δt must be limited to values below 1 s to avoid an ambiguous resistance–temperature relation and a distinction of pulses with respect to current direction and amplitude.

The effects of rising ($I_{p,r}$) and falling ($I_{p,f}$) pulses for charging and discharging currents with 1.0 C are depicted in the second row of Fig. 3. There is a minimal difference in $R_{DC,\Delta t}$ for the short Δt (1 ms and 10 ms) in Fig. 3d and Fig. 3e for the majority of the SOC range. The deviations merely increase at 10 °C and a SOC below 10 %. Since the pulses are too short, the influence of the open-circuit-voltage (OCV) is not relevant for the difference. However, in the case where $R_{DC,\Delta t}$ is calculated from $I_{p,r}$ pulses (solid lines), the system starts from an equilibrated state with no concentration gradient in the cell, since no current was applied for 1 h. In the case of $R_{DC,\Delta t}$ calculated from $I_{p,f}$ pulses (dashed lines), the current is flowing prior to the pulses and the electrode surface of the cell is already polarized [63]. When the pulse is turned off, the system returns to the equilibrium state and the concentration gradient, which was built up before, is reduced. This difference in Li-ion concentration between the $I_{p,r}$ and $I_{p,f}$ pulses results in a small overpotential difference and might be cause for the

difference in $R_{DC,\Delta t}$ [60]. The effect increases with increasing Δt in Fig. 3f, again particularly at 10 °C and a SOC below 20 %. With respect to temperature estimation, this again means that as long as Δt is small enough, excitation and idle pulses have a negligibly small influence on the resulting $R_{DC,\Delta t}$, such as in the case for pulse current direction and amplitude.

The last investigated factor is the pulse shape altered by changing the rise and fall time $t_{r/f}$ of the pulses, as depicted in Fig. 3g to Fig. 3i. This is achieved by comparing the rectangular pulses with the pulses having a larger rise/fall-time at the moment when $t_{r/f} = \Delta t$. For the sake of clarity only rising pulses with 1.0 C are compared. The markers for the pulses are the same as before, only the difference in the rise/fall-time is indicated by the color of the markers. In Fig. 3g the DC-resistances for $t_{r/f} = \Delta t = 400$ ms are compared. The pulses with instantaneous current rise (black markers) show a slight increased resistance compared to the ones with $t_{r/f} = 400$ ms (green markers), especially in the peripheral SOC regions and at lower temperatures. This is probably caused by the difference in charge-throughput for the different pulses. In general, the charge-throughput of the pulses can be calculated by integrating the current pulses:

$$Q = \int I(t)\,dt \tag{1}$$

For rectangular pulses ($t_{r/f} = 0.0$ s) the integral can be simplified to

$$Q_R = I \cdot \Delta t \tag{2}$$

For pulses with $t_{r/f} > 0.0$ s the integral can either be simplified to

$$Q_T = \frac{1}{2} I \cdot \Delta t \text{ for } \Delta t \leq t_{r/f}$$
$$\text{or to} \tag{3}$$
$$Q_T = \frac{1}{2} I \cdot t_{r/f} + I \cdot (\Delta t - t_{r/f}) \text{ for } \Delta t > t_{r/f}.$$

Comparing the different pulses in Fig. 3g, where $\Delta t = t_{r/f} = 400$ ms, the charge-throughput of the rectangular pulses is twice as large as the one of the pulses with $t_{r/f} = 400$ ms. Therefore, the polarization and ultimately the resistance is larger as well. Fig. 3h shows the same effect for the pulses with $t_{r/f} = 4.0$ s (cyan markers) at $\Delta t = t_{r/f} = 4.0$ s. The relative ratio in charge-throughput in Fig. 3h is still twice as much as the one for the pulses with $t_{r/f} = 400$ ms in Fig. 3g. However, since $t_{r/f} = 4.0$ s in Fig. 3h is ten times longer than $t_{r/f} = 400$ ms in Fig. 3g, the absolute difference in charge-throughput is larger, and the resistance difference is more apparent in Fig. 3h. When Δt is increased above $t_{r/f}$ the relative difference in charge-throughput diminishes and the difference of the DC-resistances as well. This is illustrated by increasing Δt to 8000 ms in Fig. 3i. Here, the relative charge-throughput for the pulses with $t_{r/f} = 0.0$ s compared to the pulses with $t_{r/f} = 400$ ms amounts to $\frac{Q_T}{Q_R} = \frac{7.8}{8}$ and compared to the pulses with $t_{r/f} = 4.0$ s to $\frac{Q_T}{Q_R} = \frac{6}{8}$. For this reason, the curves for $t_{r/f} = 0.0$ s and 0.4 s already overlap and the distance to the curve for $t_{r/f} = 4.0$ s is reduced. In the context of temperature estimation this suggests that as long as Δt is longer than the rise/fall-time, the pulse shape has a minor influence on the resulting $R_{DC,\Delta t}$.

After analyzing temperature, SOC and shape influence on the DC-resistance in this and the previous section, the following conclusions can be drawn for the estimation method:

- The temperature estimation method has to fit the non-linear temperature behavior of the cell.
- Δt must be short enough ($\Delta t < 1$ s) to avoid a pulse edge, direction and amplitude distinction.
- Δt must be larger than $t_{r/f}$ of the pulses occurring in the application to minimize the influence of the rise/fall-time.
- Besides temperature, only the SOC remains as an influence factor. All other factors, the current direction, the current amplitude and the rise/fall-time, have a negligible influence.

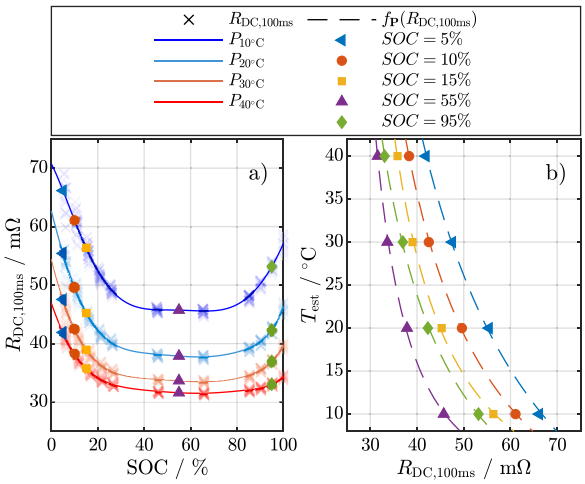

Fig. 4. Temperature estimation function example. Calculated $R_{DC,\ 100\ ms}$ and polynomial fits $P_T(SOC)$ for all experimental cells (a). Temperature estimation function fit for marked example SOC points $SOC = 5/10/15/55/95\,\%$ (b).

As a result, this leaves the corridor $t_{r/f} < \Delta t < 1$ s for the resistance-calculation-period Δt, in which acceptable sampling rates for a BMS are possible and a large variety of pulses can be used for a robust temperature estimation method without any differentiation of the pulse shape. Nonetheless, the questions still remain: what kind of estimation function should be used and which resistance-calculation-period and which pulse parameter combination is optimal for the parametrization.

3.2. Temperature estimation function

This section describes the proposed temperature estimation function (TEF) and the way it is parameterized. Since only four temperature and eleven SOC points were investigated, the goal is to find a continuous functional description of the DC-resistance for any SOC and temperature. Looking at the volume of tested pulse parameters and their possible combinations, a simplified way to represent a subset of pulse parameters $\mathbf{S_i}$, used for the parametrization of the TEF, is needed. In this regard a specific subset $\mathbf{S_i}$ contains all $R_{DC,\Delta t}$, which can be calculated from all pulses meeting the selection criteria. The different subsets of $R_{DC,\Delta t}$ are then approximated by a SOC-dependent polynomial $P_T(SOC)$ of 8th degree described by Eq. (4) for a certain Δt and for a specific experimental temperature $T \in [10\,°C, 20\,°C, 30\,°C, 40\,°C]$.

$$P_T(SOC) = \sum_{i=0}^{8} x_i \cdot SOC^i \approx R_{DC,\Delta t}(SOC, T) \tag{4}$$

Fig. 4a serves as an example representing the polynomials for $R_{DC,\ 100\ ms}$ fitted to a subset of pulses $\mathbf{S_i}$. In this case, $\mathbf{S_i}$ includes rising and falling pulses with ±0.5 C and ±1.0 C for $t_{r/f} = 0.0$ s of all cells from Table 1. An overview of all tested subsets can be found in Fig. 5. In the example in Fig. 4a, all calculated DC-resistances from the subset are marked with '×' in the temperature related color. The resulting polynomial fit for each temperature is represented by a solid line. To retrieve the temperature from the four polynomial representations, the resistance values at the specific SOC are evaluated for each temperature. These four points are represented by the vector $\mathbf{P}(SOC)$ in Eq. (5):

$$\mathbf{P}(SOC) = \begin{pmatrix} P_{10\,°C}(SOC) \\ P_{20\,°C}(SOC) \\ P_{30\,°C}(SOC) \\ P_{40\,°C}(SOC) \end{pmatrix} \tag{5}$$

The markers, except for '×' in Fig. 4a and Fig. 4b, depict the resistance–temperature relation for the vector $\mathbf{P}(SOC)$ for exemplary SOC points.

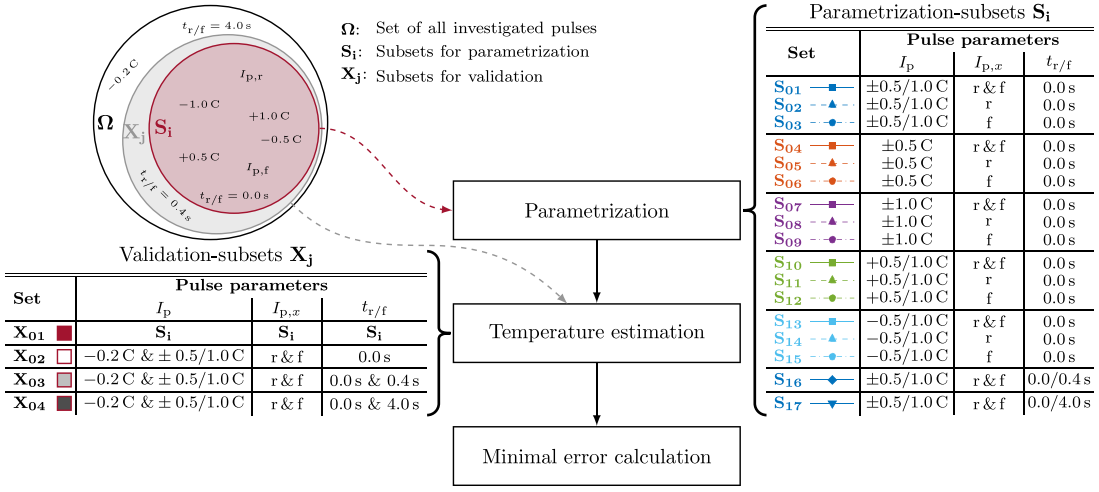

Validation-subsets $\mathbf{X_j}$

Set	Pulse parameters I_p	$I_{p,x}$	$t_{r/f}$
$\mathbf{X_{01}}$	$\mathbf{S_i}$	$\mathbf{S_i}$	$\mathbf{S_i}$
$\mathbf{X_{02}}$	−0.2 C & ±0.5/1.0 C	r & f	0.0 s
$\mathbf{X_{03}}$	−0.2 C & ±0.5/1.0 C	r & f	0.0 s & 0.4 s
$\mathbf{X_{04}}$	−0.2 C & ±0.5/1.0 C	r & f	0.0 s & 4.0 s

Parametrization-subsets $\mathbf{S_i}$

Set	Pulse parameters I_p	$I_{p,x}$	$t_{r/f}$
$\mathbf{S_{01}}$	±0.5/1.0 C	r & f	0.0 s
$\mathbf{S_{02}}$	±0.5/1.0 C	r	0.0 s
$\mathbf{S_{03}}$	±0.5/1.0 C	f	0.0 s
$\mathbf{S_{04}}$	±0.5 C	r & f	0.0 s
$\mathbf{S_{05}}$	±0.5 C	r	0.0 s
$\mathbf{S_{06}}$	±0.5 C	f	0.0 s
$\mathbf{S_{07}}$	±1.0 C	r & f	0.0 s
$\mathbf{S_{08}}$	±1.0 C	r	0.0 s
$\mathbf{S_{09}}$	±1.0 C	f	0.0 s
$\mathbf{S_{10}}$	+0.5/1.0 C	r & f	0.0 s
$\mathbf{S_{11}}$	+0.5/1.0 C	r	0.0 s
$\mathbf{S_{12}}$	+0.5/1.0 C	f	0.0 s
$\mathbf{S_{13}}$	−0.5/1.0 C	r & f	0.0 s
$\mathbf{S_{14}}$	−0.5/1.0 C	r	0.0 s
$\mathbf{S_{15}}$	−0.5/1.0 C	f	0.0 s
$\mathbf{S_{16}}$	±0.5/1.0 C	r & f	0.0/0.4 s
$\mathbf{S_{17}}$	±0.5/1.0 C	r & f	0.0/4.0 s

Fig. 5. Flowchart depicting the steps for finding error minimum for different combination of parametrization- and validation-subsets. Next to the parametrization- and validation-subsets names, their marking/color scheme is depicted to explicitly distinguish them.

Since $\mathbf{P}(SOC)$ only represent the temperature related to four resistance values, an approximation function is needed for the resistance values outside and in between these points. To describe the non-linear behavior between DC-resistance and temperature, an exponential function was selected. The estimation function $f_\mathbf{P}$ in Eq. (6) maps the resistance–temperature behavior for each vector $\mathbf{P}(SOC)$ at a specific SOC
point.

$$T_{est} = f_\mathbf{P}(R_{DC,\Delta t}) = A \cdot e^{\frac{B}{R_{DC,\Delta t}}} + C \tag{6}$$

The temperature T_{est} is the temperature estimated with $f_\mathbf{P}$ and the function variables A, B and C are SOC-dependent parameters fitted to each vector $\mathbf{P}(SOC)$. The dashed lines in Fig. 4b represent $f_\mathbf{P}$ for the exemplary SOC points from Fig. 4a. The corresponding course of the function variables is depicted in Fig. S2.

3.3. Parametrization- and validation-subsets

After determining the TEF, the next step is to find suitable subsets of pulses for the parametrization of $f_\mathbf{P}$ and the corresponding Δt for temperature estimation. To achieve this, the flowchart in Fig. 5 is used. The circles on the left hand side of Fig. 5 represent different subsets of pulses containing specific parameters, where $\boldsymbol{\Omega}$ is the set containing all pulses. In the following, two different type of subsets of $\boldsymbol{\Omega}$ will be distinguished. The first type are parametrization-subsets $\mathbf{S_i}$, used to parameterize $f_\mathbf{P}$. The second type are validation-subsets $\mathbf{X_j}$, used to determine the accuracy and optimal Δt of the parametrization-subsets. This is done in the three steps depicted in the center of Fig. 5. In the first step, different subsets $\mathbf{S_i}$ taken from all pulses are used to parameterize the polynomial representation according to Eq. (4). The 17 validation-subsets used in this work are depicted in the table on the right of Fig. 5, including the pulse parameters contained in the subsets. The polynomials $P_T(SOC)$ are generated for each of the 17 subsets for Δt reaching from 1 ms to 10 s. In the second step, the TEF of Eq. (6) is used to estimate the temperature for the pulses of the four validation-subsets $\mathbf{X_j}$ in the table on the left of Fig. 5. Each validation-subset tests a specific property, which will be described in the discussion of Figs. 6 and 7. In the third step, the suitability for temperature estimation of the parametrization-subsets $\mathbf{S_i}$ is determined for each validation-subset $\mathbf{X_i}$. As a measure for the suitability, the root mean square error (RMSE) is calculated according to Eq. (7).

$$\mathrm{RMSE}_{\mathbf{S_i}}(\mathbf{X_j}) = \sqrt{\frac{1}{|\mathbf{X_j}|}\sum_{x\in\mathbf{X_j}}(T_{est,x} - T_{m,x})^2} \tag{7}$$

$T_{est,x}$ is the temperature estimated with $f_\mathbf{P}$ for each resistance value calculated from the pulses in the validation-subset $\mathbf{X_j}$ and $T_{m,x}$ is the measured temperature during the experiment. Finally, the minimal RMSE according to Eq. (8) is utilized to find the most suitable resistance-calculation-period Δt in each subset $\mathbf{S_i}$ for each $\mathbf{X_j}$.

$$\mathrm{RMSE}_{\mathbf{S_i}}(\mathbf{X_j})_{min} = \min_{\Delta t\in[10^{-3}\ \mathrm{s},10\ \mathrm{s}]} \mathrm{RMSE}_{\mathbf{S_i}}(\mathbf{X_j}) \tag{8}$$

3.4. Optimal parametrization-subset and resistance-calculation-period

The results of the error calculation for the different parametrization- and validation-subsets are discussed in this section. Fig. 6 depicts the results for the validation with $\mathbf{X_{01}}$ (left column), where parametrization- and validation-subset are equal, and $\mathbf{X_{02}}$ (right column), where all pulses with $t_{r/f} = 0.0$ s are included. The figure investigates the influence of the pulse parameters on the TEF, when only pulses with a rise/fall-time $t_{r/f} = 0.0$ s are considered. Fig. 6a and Fig. 6b exemplary depict the course of the RMSE over the resistance-calculation-period for the corresponding validation-subsets. For short Δt all subsets indicate an increased error, followed by an error decline and leading to a more or less distinct error plateau with increasing Δt. By increasing Δt further, the error shows a steeper increase leading to a linear course with a constant slope.

In Fig. 6a the validation-subset $\mathbf{X_{01}}$ is equal to the individual parametrization-subsets $\mathbf{S_i}$. This represents an application case, where all load changes are known prior to the parametrization of the TEF. For the sake of clarity, not all 15 parametrization-subsets are depicted. For $\mathbf{X_{02}}$ in Fig. 6b all pulses with a rise/fall-time $t_{r/f} = 0.0$ s and additionally pulses with −0.2 C, unknown to the parametrization-subsets, are included. Since the parametrization-subsets stay the same, they only partly include the pulses of the validation-subset. This represents an application case, where not all of the load changes are known prior to the parametrization of the TEF. The general shape of the error course is not influenced compared to Fig. 6a, but all curves show an increased error course and error minima. Again, only exemplary curves are depicted for the sake of clarity.

In the pulse shape analysis in Section 3.1.2, it is assumed that the optimal resistance-calculation-period is located in between the boundaries of $t_{r/f} < \Delta t < 1$ s. This assumption is confirmed considering Fig. 6c and Fig. 6d. For $\mathbf{X_{01}}$ in Fig. 6c, where the validation- and parametrization-subset are equal, the majority of the error minima are located in between 13 ms to 95 ms. The only exceptions are the error minima for $\mathbf{S_{11}}$ and $\mathbf{S_{12}}$ at 800 ms and 830 ms, respectively. The minimal RMSE for the subsets are within 0.95 K and 1.18 K. Part of this error

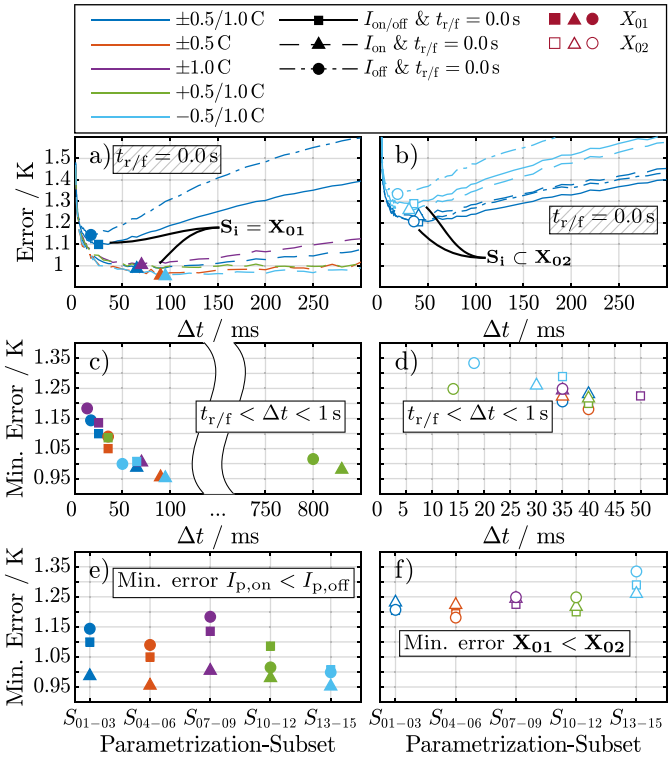

Fig. 6. Error behavior of the different parametrization-subsets validated with $\mathbf{X_{01}}$, where the validation- and parametrization-subset are equal, and $\mathbf{X_{02}}$, including all pulses with $t_{r/f}$ = 0.0 s. Exemplary error course over Δt for $\mathbf{X_{01}}$ (a) and $\mathbf{X_{02}}$ (b). Resistance-calculation-period of error minima of the parametrization-subsets validated with $\mathbf{X_{01}}$ (c) and $\mathbf{X_{02}}$ (d). Comparison of the minimal error of the different parametrization-subsets for $\mathbf{X_{01}}$ (e) and $\mathbf{X_{02}}$ (f). The markers represent the minimum error of the parametrization-subsets. Table S1 in the supplementary gives a detailed overview with the RMSE minima and the related resistance-calculation-periods for all parametrization- and validation-subsets.

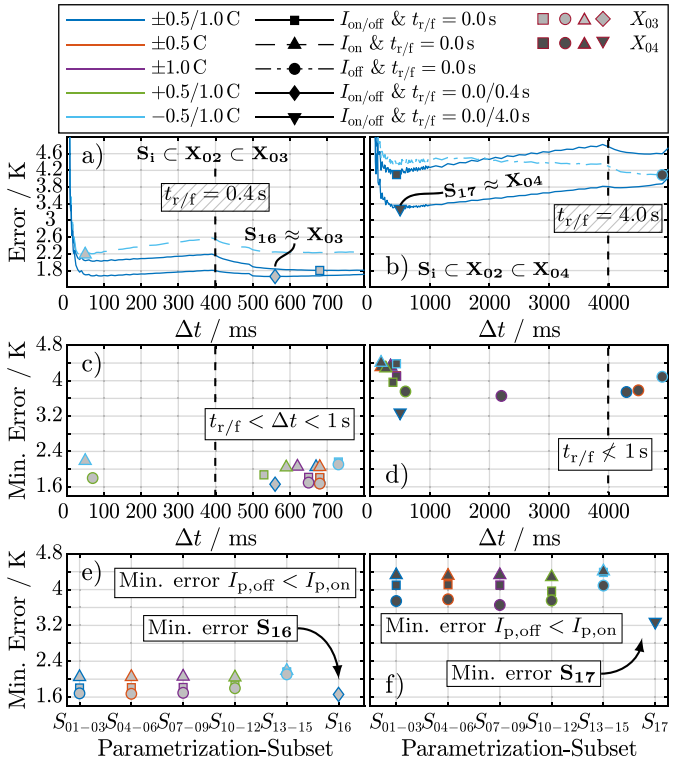

Fig. 7. Error behavior of the different parametrization-subsets validated with $\mathbf{X_{03}}$, including the same pulses as $\mathbf{X_{02}}$ and all pulses with $t_{r/f}$ = 0.4 s, and $\mathbf{X_{04}}$, including the same pulses as $\mathbf{X_{02}}$ and all pulses with $t_{r/f}$ = 4.0 s. Exemplary error course over Δt for $\mathbf{X_{03}}$ (a) and $\mathbf{X_{04}}$ (b). Resistance-calculation-period of error minima of the parametrization-subsets validated with $\mathbf{X_{03}}$ (c) and $\mathbf{X_{04}}$ (d). Comparison of the minimal error of the different parametrization-subsets for $\mathbf{X_{03}}$ (e) and $\mathbf{X_{04}}$ (f). Table S1 in the supplementary gives a detailed overview with the RMSE minima and the related resistance-calculation-periods for all parametrization- and validation-subsets.

is related to the generation of the TEF. Since the TEF is generated from the average values of the three cells in Table 1, the TEF is not perfectly adjusted to a specific cell and the error minima is partly caused by the resistance variation between the cells. To improve the estimation method, a procedure, which adjusts the TEF to specific cells, is introduced later in Section 3.5. For validation-subset $\mathbf{X_{02}}$ in Fig. 6d, the range for the optimal resistance-calculation-period is even smaller. The minimal RMSE for the subsets are within 1.18 K and 1.33 K and below 50 ms.

Fig. 6e and Fig. 6f are utilized to judge if a specific combination of pulse parameters is beneficial for the parametrization. For validation-subset $\mathbf{X_{01}}$ in Fig. 6e, the parametrization-subsets including only pulses with rising edges $I_{p,r}$, have smaller minimal errors compared to those including the same pulses with falling edges $I_{p,f}$. This might be caused by the fact that rising pulses start from an idle state and no concentration gradients are present in the cell. Whereas falling pulses start from a previously polarized cell. The reduced error for parametrization-subsets with rising pulses is no longer present for validation-subset $\mathbf{X_{02}}$ in Fig. 6f. Here, no specific parametrization seems to be advantageous and the error minima are higher compared to $\mathbf{X_{01}}$.

Fig. 7 investigates the influence of the rise/fall-time, utilizing the validation-subsets $\mathbf{X_{03}}$ and $\mathbf{X_{04}}$. As in Fig. 6, each column of Fig. 7 represents the results for one validation-subset. Additionally to the 15 parametrization-subsets as seen in Fig. 6, the subsets $\mathbf{S_{16}}$ and $\mathbf{S_{17}}$ are added to the parametrization-subsets in Fig. 7, containing pulses with the same rise/fall-time as the corresponding validation-subsets $\mathbf{X_{03}}$ and $\mathbf{X_{04}}$.

Fig. 7a and Fig. 7b exemplary depict the course of the RMSE over Δt. By adding the pulses with $t_{r/f}$ = 0.4 s and 4.0 s to the validation-subsets, a second error decline evolves after Δt passes $t_{r/f}$. Since the amount of pulses differing from the parametrization-subsets increases, the general RMSE increases as well, especially for validation-subset $\mathbf{X_{04}}$ in Fig. 7b, which includes the pulses with $t_{r/f}$ = 4.0 s. Nevertheless, the parametrization-subsets $\mathbf{S_{16}}$ and $\mathbf{S_{17}}$, including the pulses with the corresponding rise/fall-time of the validation-subsets, show the lowest error course.

The minimal RMSE of the parametrization-subsets and the corresponding resistance-calculation-periods for $\mathbf{X_{03}}$ and $\mathbf{X_{04}}$ are depicted in Fig. 7c and Fig. 7d. The assumption for the minimal error corridor $t_{r/f} < \Delta t < 1$ s holds for the majority of the parametrization-subsets in Fig. 7c. However, the two subsets $\mathbf{S_{12}}$ and $\mathbf{S_{14}}$ violate the assumption. The reason can be seen in Fig. 7a, by observing the error course for $\mathbf{S_{14}}$ (dashed line). The error increase after the first error plateau is steeper than for the other parametrization-subsets and therefore the second error decline after Δt passes $t_{r/f}$ = 0.4 s does not fall below the first one. This results in an error minimum, which occurs at $\Delta t < t_{r/f}$. For all other parametrization-subsets in Fig. 7c, the resistance-calculation-period with the minimal RMSE lies between 530 ms and 730 ms. For the RMSE minima in Fig. 7d the assumption cannot be fulfilled, since $t_{r/f}$ = 4.0 s > 1 s. Therefore, there are error minima above 4.0 s, below 1 s and even in between, with the majority of the error minima below 1 s.

Fig. 7e and Fig. 7f are utilized to judge if a specific combination of pulse parameters is beneficial for the parametrization. In contrast to validation-subset $\mathbf{X_{01}}$ in Fig. 6e, the parametrization-subsets including falling pulses $I_{p,f}$ have a smaller minimal error compared to those

including the same pulses with rising pulses $I_{p,r}$ for validation-subset $\mathbf{X_{03}}$ in Fig. 7e. As already noted in Fig. 7a, parametrization-subset $\mathbf{S_{16}}$, including the pulses with $t_{r/f} = 0.4\,s$, has the smallest minimal RMSE (1.66 K) for $\mathbf{X_{03}}$. Except for the generally higher minimal RMSE, the statements of Fig. 7e are transferable to Fig. 7f. Here, parametrization-subset $\mathbf{S_{17}}$, including the pulses with $t_{r/f} = 4.0\,s$, has the smallest minimal RMSE (3.28 K) for $\mathbf{X_{04}}$. Bringing all findings together, the optimal subsets have to fulfill the following requirements:

- The closer the parametrization pulses are to the actual pulses occurring in the application, the smaller the estimation error.
- If only rectangular pulses occur in the application, the optimal resistance-calculation-period can be found below 1 s.
- If pulses with $t_{r/f} > 0.0\,s$ occur in the application, the optimal resistance-calculation-period Δt for the TEF is longer than $t_{r/f}$. However, pulses with long $t_{r/f}$ should be excluded from the temperature estimation, because of the increasing error caused by the DC-resistance dependence on pulse shape for increasing Δt (Section 3.1).

3.5. Validation experiment

To validate the results of the last two sections for conditions close to an application, the TEF was tested with the experimental setup shown in Fig. 2. The pulses in the current-profile (Fig. 2b) for the validation are more extensive than the ones used for the subsets to generate the TEFs. In addition to unknown pulse amplitudes, the current-profile also contains pulses, not starting from and not returning to an idle state. Besides, the current-profile rarely includes resting periods, which are relatively short compared to the resting period of 1 h before each reference pulse. Even if a linear polarization behavior for the relevant time domain ($\Delta t < 1\,s$) and current range is assumed, the current-profile is only partly utilizable for temperature estimation. To take extensive and irregular pulses of a current-profile into account and to incorporate the findings from the last section, the pulse filter with three conditions in Fig. 8a is introduced. The first condition excludes pulses with long $t_{r/f}$, causing increased errors such as for $t_{r/f} = 0.4\,s$ and small current changes by accepting only pulses which have an absolute current change rate $|\Delta I_{r/f}|$ within $t_{r/f}$ larger than a minimal change rate ΔI_{min}. In the validation experiment, two minimal change rates are evaluated: $\Delta I_{min} = 0.2\,C$ to achieve conditions similar to $\mathbf{X_{02}}$ and $\Delta I_{min} = 0.1\,C$ to have a validation scenario with pulses differing even more from the parametrization-subset than in $\mathbf{X_{02}}$. The second condition ensures that there is no current direction change during $t_{r/f}$. After $t_{r/f}$ the pulse should hold a stable current value till Δt is reached. To ensure this, the third condition limits the current fluctuation to stay within the tolerance ΔI_{tol}. For the validation experiment, ΔI_{tol} was set to 10 mA to avoid the influence of the HPS current sampling precision. If all three conditions are fulfilled, the pulse is used to calculate a $R_{DC,\Delta t}$. To determine the other filter parameters, as well as Δt and $\mathbf{S_i}$ for the validation experiment, the sampling rate of the test system, the module current, and its current changes had to be considered. The maximal sampling rate of 200 Sample/s was applied to the test equipment. Nevertheless, the first valid data point, after a current change, is sampled after 100 ms, if current-profiles are a part of the test sequence. For this reason Δt had to be longer than 100 ms and the limit for $t_{r/f}$ was set to 100 ms. Assuming the current changes are known for the application, the selection of a suitable subset $\mathbf{S_i}$ can be accomplished by analyzing the current change distribution. The module current contained charge and discharge pulses with the majority of current changes in the regime of 0.4 C and less (Fig. S1). The closest error behavior for these kind of pulses is represented by validation-subset $\mathbf{X_{02}}$ and parametrization-subset $\mathbf{S_{04}}$, which shows the best congruence in pulse parameters with the module current-profile. According to Fig. 6c, the optimal resistance-calculation-period for $\mathbf{S_{04}}$ and $\mathbf{X_{02}}$ is $\Delta t = 40$ ms. Nevertheless, Δt is set to 120 ms to fulfill the condition $t_{r/f} < \Delta t < 1\,s$. The RMSE of 1.26 K for $\mathbf{S_{04}}$ at this resistance-calculation-period is still relatively close to the minimal RMSE of 1.18 K for $\mathbf{S_{06}}$.

Table 4
Settings for the algorithm used for the method validation in Fig. 8a and the estimation error results for each cell in the validation module for the corresponding setting.

Parameter	Value					
$\mathbf{S_i}$/–	$\mathbf{S_{04}}$					
Δt/ms	120					
$t_{r/f}$/ms	100					
ΔI_{min}/C	0.1/0.2					
ΔI_{tol}/mA	10					
Cell	C_4	C_5	C_6	C_7	C_8	C_9
$R_{DC,offset}$ [a]/mΩ	2.31	2.18	2.41	1.83	2.51	2.74
$RMSE_{S04}(0.1C)$ [b]/K	1.11	0.96	1.08	0.96	1.01	0.97
$RMSE_{S04}(0.2C)$ [b]/K	0.93	0.65	0.90	0.59	0.67	0.77

[a] Calculated at 25 °C, SOC = 50 % and Δt = 120 ms.
[b] $RMSE_{S_i}(\Delta I_{min})$ calculated according to Eq. (4).

In general, the resistance of cells slightly differ, even if they are from the same production batch and are treated equally. This is also the case for the cells used in the pulse experiment (Table 1) and the validation experiment (Table 3). Since the function variables of the TEF in Eq. (6) are fitted to the average of the pulse experiment cells, a correction is needed to make the TEF applicable to the validation experiment cells. Since the shape of the DC-resistance curves of the cells used in the pulse experiment only differed by an offset, the correction is achieved by adding an individual offsets $R_{DC,offset}$ to each cell of the validation experiment before applying the TEF. The offset is determined with the pulses used to calculate the $R_{DC,10\,s}$ in Table 3 at SOC = 50 % and 25 °C, though evaluated for $\Delta t = 120$ ms instead of 10 s. At this temperature and SOC the influence of any pulse parameter is minimal, which makes the offset correction more robust. The difference between the $R_{DC,120\,ms}$ of each experimental cell and the resistance calculated by the inverse function of $f_{\mathbf{P}}$ for SOC = 50 % and 25 °C results in the offset $R_{DC,offset}$. An overview of all settings for the pulse filter, the offset values and the results of the validation experiment for each cell is listed in Table 4. The offset values $R_{DC,offset}$ reaching from 1.83 mΩ to 2.74 mΩ seem to be quite high in relation to the DC-resistance of the cells in Table 3. However, according to the $R_{DC,10\,s}$ distribution for the same cell measured by Zilberman et al. [31], the cells used in the 6s1p-module are from the lower end of the DC-resistance range of the investigated cell and the cells used for the pulse experiment are from the upper end, leading to this relatively high offset values.

After the offset correction, the final step is applied to the $R_{DC,120\,ms}$ in Fig. 8a. If several $R_{DC,120\,ms}$ are calculated within a window t_w = 10 s, the values are averaged and only one temperature estimation is performed. This reduces the influence of outliers and decreases the estimation error. The only missing variable for the TEF is the SOC of each cell. To determine the SOC, the coulomb counting method is applied [64–67]. The initial state-of-charge SOC_0 was determined by utilizing the relation between the SOC and the OCV. The coulombic efficiency for charging/discharging the cell was assumed to be one. The values for the actual capacity C_{act} of each cell were taken from Table 3.

Fig. 8b shows the measured cell temperature T_m of cell C_9 in the module and serves as example to visualize the estimated temperatures for two different pulse current change limits ΔI_{min}. Since more pulses were valid for the temperature estimation with $\Delta I_{min} = 0.1\,C$, the temperature is continuously estimated during the load profile. Whereas the temperature estimation for $\Delta I_{min} = 0.2\,C$ shows gaps of up to 10 min between two estimation points. The estimation error $RMSE_{S_{04}}(\Delta I_{min})$ for $\Delta I_{min} = 0.1\,C$ is higher for each cell than for 0.2 C (Table 4). An increased estimation error is visible for $\Delta I_{min} = 0.1\,C$, especially at the 2 h mark in Fig. 8b. At this point, the current-profile of Fig. 2b shows only small current changes close to the current change limit. However, the error of each cell is smaller than the minimal RMSE for any $\mathbf{S_i}$

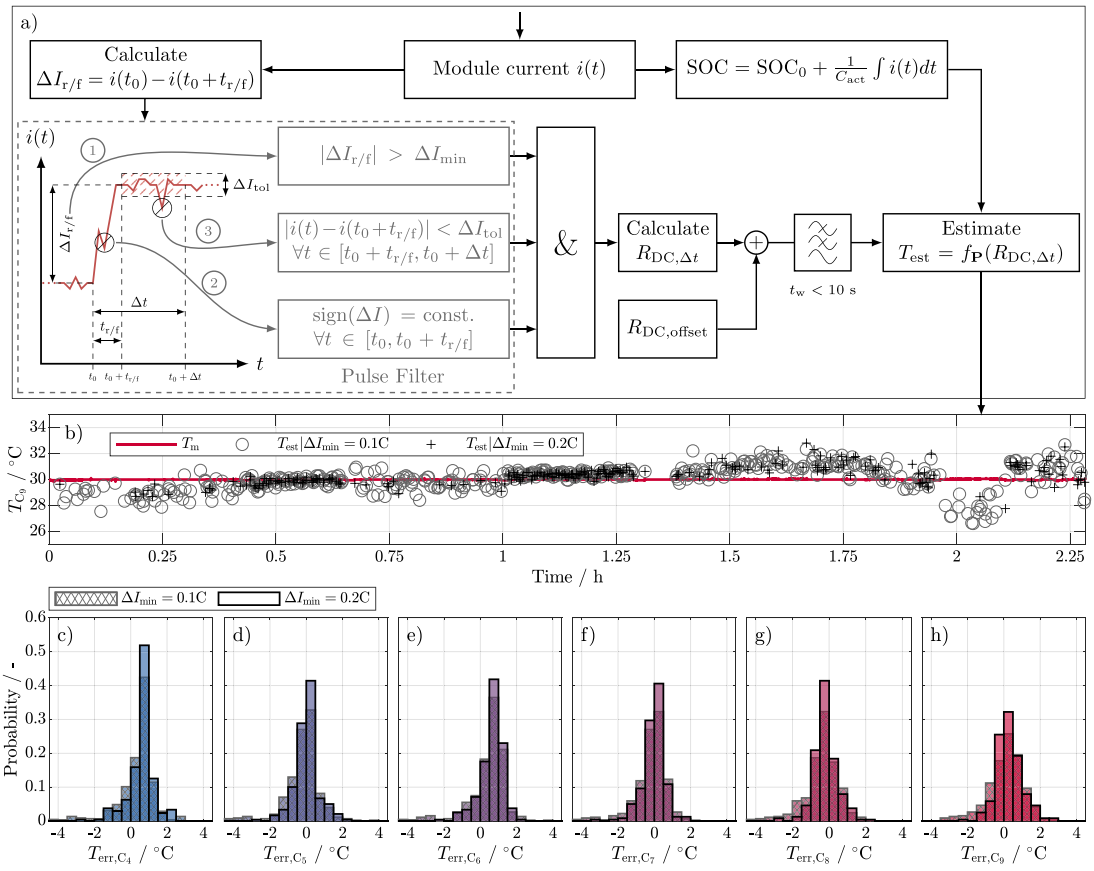

Fig. 8. Algorithm for the method validation with pulse filter (a). Exemplary temperature estimation results for cell C_9 with two different pulse filter settings and corresponding measured cell temperature (b). Error probability for each module cell for the two different pulse filter settings (c–h).

validated with $\mathbf{X_{02}}$. The RMSE for $\Delta I_{min} = 0.1$ C are between 0.96 K and 1.11 K. For $\Delta I_{min} = 0.2$ C the RMSE ranges between 0.59 K and 0.93 K. The detailed estimation error probability for each cell in the module is depicted in Fig. 8c to Fig. 8h, showing that the majority of the estimation errors are within ±1 K for any cell.

Although the method was validated with unknown cells, it was only validated for newly acquired cells. Since aging influences the impedance and capacity of a cell [4,30,68], the estimation method needs to be adapted over the application lifetime, in particular for increasing non-linear battery behavior towards the end of life. A possible approach to solve this issue is already part of the module validation. By updating the offset correction $R_{DC,offset}$ of each cell, aging induced impedance changes could be compensated. To get the offset values, the battery has to be in an idle state without any temperature or SOC discrepancy, such as a parking EV after being charged and balanced. In this case only one temperature sensor for the whole battery pack is needed, serving as a reference. Before the application is used again, an intentional pulse, for example triggered by the battery charger, can be utilized to calculate the new offset correction. A randomized pulse, such as caused by turning on the EV, can be considered to calculate the new offset correction as well. Nevertheless, further investigations are necessary to validate this approach, since it assumes a resistance increase, which is uniform over the whole SOC range. Along with the compensation of the DC-resistance, an accurate SOC estimation over lifetime is significant for the estimation method. To achieve this, a more sophisticated SOC estimator [69,70] than the coulomb counter used for the validation is required, especially tracing the capacity fade with an accurate SOH estimator.

Another issue occurs for systems with parallel connected cells. If the current distribution is known and is not affected by the connection itself, the temperature estimation method of this work can be applied without limitations. In this case, it is possible to calculate the individual DC-resistances of each cell in the parallel connection and estimate the temperature with the TEF. However, further experiments are needed to investigate and validate this assumption. If the current distribution is unknown, which is usually the case, the estimation method cannot determine the temperature of each cell.

4. Conclusion

In this work, an online temperature estimation method based on DC-resistance $R_{DC,\Delta t}$ is proposed. Unlike previous studies, the method does neither rely on a transformation of the pulses to the frequency domain nor on additional equipment for excitation. The method entirely relies on the current and voltage signals in the time domain generated by the application, even considering deviations from the ideal edges of a pulse. To investigate the temperature behavior and the underlying processes in the time domain, the pulse based DC-resistance values $R_{DC,\Delta t}$ were regarded for a variety of pulse shapes and Δt. Based on the results, an estimation method was proposed and benchmarked for various combinations of pulse subsets and Δt from 1 ms to 10 s. The results showed that there is not the one optimal combination of pulses and Δt for the proposed estimation method. The following facts have to be considered to find the optimal combination:

– As long as Δt is short enough, avoiding a major influence of DC-resistance spread at low SOC and temperatures, the different pulse parameters (pulse amplitude, pulse direction and rising/falling pulse) have a negligible influence on the estimation result, making the estimation method independent of the pulse shape. However, the dependence on SOC still remains. If Δt is too short, the estimation error increases. In the remaining intermediate

time domain from approximately 10 ms to several 100 ms, the estimation error has its minimum and shows only a slight error increase. For the investigated cell, the minimal RMSE amounts to 0.95 K for $\Delta t = 95$ ms.

- If the current change of the pulse does not happen instantaneously, but rises/falls till reaching a steady value, the estimation method is also applicable as long as Δt is longer than the rise/fall-time $t_{r/f}$ of the pulse. Nevertheless, for an acceptable estimation error, $t_{r/f}$ and Δt are limited. For the investigated cell, the shortest verified rise/fall-time $t_{r/f}$ for a non-rectangular excitation pulse is 0.4 s with a minimal RMSE of 1.66 K for $\Delta t = 560$ ms.
- The validation on the module level showed that the method can be applied to serial connected cells. By filtering the pulses occurring in the continuous current-profile and adjusting the calculated DC-resistance with a simple offset $R_{DC,offset}$ to the cells of the module, the RMSE of each cell was reduced to less than 1 K (Table 4).

Although the method was investigated and validated under several conditions, there are still open questions for future studies. As mentioned at the end of the discussion, the influence of aging on the estimation method and application of the estimation method to parallel connected cells are the most urgent ones. In addition, the validity for other cell chemistries and the behavior for other thermal boundary conditions, like a changing temperature gradient during cycling, are of interest.

CRediT authorship contribution statement

S. Ludwig: Conceptualization, Methodology, Software, Project administration, Writing - original draft, Visualization, Data curation, Investigation, Writing - review & editing. **I. Zilberman:** Conceptualization, Writing - review & editing. **M.F. Horsche:** Conceptualization, Writing - review & editing. **T. Wohlers:** Software, Investigation. **A. Jossen:** Writing - review & editing, Supervision.

Declaration of competing interest

The authors declare that they have no known competing financial interests or personal relationships that could have appeared to influence the work reported in this paper.

Acknowledgment

This work has received funding from the European Union's Horizon 2020 research and innovation programme under the grant 'Electric Vehicle Enhanced Range, Lifetime And Safety Through INGenious battery management' [EVERLASTING-713771].

Appendix A. Supplementary data

Supplementary material related to this article can be found online at https://doi.org/10.1016/j.jpowsour.2021.229523.

References

[1] S. Ma, M. Jiang, P. Tao, C. Song, J. Wu, J. Wang, T. Deng, W. Shang, Temperature effect and thermal impact in lithium-ion batteries: A review, Prog. Nat. Sci.: Mater. Int. 28 (6) (2018) 653–666, http://dx.doi.org/10.1016/j.pnsc.2018.11.002.

[2] T. Waldmann, M. Wilka, M. Kasper, M. Fleischhammer, M. Wohlfahrt-Mehrens, Temperature dependent ageing mechanisms in Lithium-ion batteries – A Post-Mortem study, J. Power Sources 262 (2014) 129–135, http://dx.doi.org/10.1016/j.jpowsour.2014.03.112.

[3] M. Naumann, M. Schimpe, P. Keil, H.C. Hesse, A. Jossen, Analysis and modeling of calendar aging of a commercial LiFePO4/graphite cell, J. Energy Storage 17 (2018) 153–169, http://dx.doi.org/10.1016/j.est.2018.01.019.

[4] S.F. Schuster, M.J. Brand, C. Campestrini, M. Gleissenberger, A. Jossen, Correlation between capacity and impedance of lithium-ion cells during calendar and cycle life, J. Power Sources 305 (2016) 191–199, http://dx.doi.org/10.1016/j.jpowsour.2015.11.096.

[5] M. Fleischhammer, T. Waldmann, G. Bisle, B.-I. Hogg, M. Wohlfahrt-Mehrens, Interaction of cyclic ageing at high-rate and low temperatures and safety in lithium-ion batteries, J. Power Sources 274 (2015) 432–439, http://dx.doi.org/10.1016/j.jpowsour.2014.08.135.

[6] A. Friesen, F. Horsthemke, X. Mönnighoff, G. Brunklaus, R. Krafft, M. Börner, T. Risthaus, M. Winter, F.M. Schappacher, Impact of cycling at low temperatures on the safety behavior of 18650-type lithium ion cells: Combined study of mechanical and thermal abuse testing accompanied by post-mortem analysis, J. Power Sources 334 (2016) 1–11, http://dx.doi.org/10.1016/j.jpowsour.2016.09.120.

[7] X.M. Xu, R. He, Research on the heat dissipation performance of battery pack based on forced air cooling, J. Power Sources 240 (2013) 33–41, http://dx.doi.org/10.1016/j.jpowsour.2013.03.004.

[8] B. Wu, V. Yufit, M. Marinescu, G.J. Offer, R.F. Martinez-Botas, N.P. Brandon, Coupled thermal–electrochemical modelling of uneven heat generation in lithium-ion battery packs, J. Power Sources 243 (2013) 544–554, http://dx.doi.org/10.1016/j.jpowsour.2013.05.164.

[9] C. Zhao, W. Cao, T. Dong, F. Jiang, Thermal behavior study of discharging/charging cylindrical lithium-ion battery module cooled by channeled liquid flow, Int. J. Heat Mass Transfer 120 (2018) 751–762, http://dx.doi.org/10.1016/j.ijheatmasstransfer.2017.12.083.

[10] A. Tang, J. Li, L. Lou, C. Shan, X. Yuan, Optimization design and numerical study on water cooling structure for power lithium battery pack, Appl. Therm. Eng. 159 (2019) 113760, http://dx.doi.org/10.1016/j.applthermaleng.2019.113760.

[11] X. Liu, W. Ai, M. Naylor Marlow, Y. Patel, B. Wu, The effect of cell-to-cell variations and thermal gradients on the performance and degradation of lithium-ion battery packs, Appl. Energy 248 (2019) 489–499, http://dx.doi.org/10.1016/j.apenergy.2019.04.108.

[12] I. Zilberman, S. Ludwig, M. Schiller, A. Jossen, Online aging determination in lithium-ion battery module with forced temperature gradient, J. Energy Storage 28 (2020) 101170, http://dx.doi.org/10.1016/j.est.2019.101170.

[13] L. Wang, D. Lu, M. Song, X. Zhao, G. Li, Instantaneous estimation of internal temperature in lithium–ion battery by impedance measurement, Int. J. Energy Res. 18 (2) (2020) 207, http://dx.doi.org/10.1002/er.5144.

[14] C. Ji, B. Wang, S. Wang, S. Pan, Du Wang, P. Qi, K. Zhang, Optimization on uniformity of lithium-ion cylindrical battery module by different arrangement strategy, Appl. Therm. Eng. 157 (2019) 113683, http://dx.doi.org/10.1016/j.applthermaleng.2019.04.093.

[15] A. Fill, S. Koch, K.P. Birke, Algorithm for the detection of a single cell contact loss within parallel-connected cells based on continuous resistance ratio estimation, J. Energy Storage 27 (2020) 101049, http://dx.doi.org/10.1016/j.est.2019.101049.

[16] R. Koch, A. Jossen, Temperature measurement of large format pouch cells with impedance spectroscopy, in: EVS28 International Electric Vehicle Symposium and Exhibition, 2015.

[17] J.P. Schmidt, S. Arnold, A. Loges, D. Werner, T. Wetzel, E. Ivers-Tiffée, Measurement of the internal cell temperature via impedance: Evaluation and application of a new method, J. Power Sources 243 (2013) 110–117, http://dx.doi.org/10.1016/j.jpowsour.2013.06.013.

[18] L. Raijmakers, D.L. Danilov, J. van Lammeren, M. Lammers, P. Notten, Sensorless battery temperature measurements based on electrochemical impedance spectroscopy, J. Power Sources 247 (2014) 539–544, http://dx.doi.org/10.1016/j.jpowsour.2013.09.005.

[19] L.H.J. Raijmakers, D.L. Danilov, J.P.M. van Lammeren, T.J.G. Lammers, H.J. Bergveld, P.H.L. Notten, Non-zero intercept frequency: An accurate method to determine the integral temperature of li-ion batteries, IEEE Trans. Ind. Electron. 63 (5) (2016) 3168–3178, http://dx.doi.org/10.1109/TIE.2016.2516961.

[20] R.R. Richardson, P.T. Ireland, D.A. Howey, Battery internal temperature estimation by combined impedance and surface temperature measurement, J. Power Sources 265 (2014) 254–261, http://dx.doi.org/10.1016/j.jpowsour.2014.04.129.

[21] R. Srinivasan, B.G. Carkhuff, M.H. Butler, A.C. Baisden, Instantaneous measurement of the internal temperature in lithium-ion rechargeable cells, Electrochim. Acta 56 (17) (2011) 6198–6204, http://dx.doi.org/10.1016/j.electacta.2011.03.136.

[22] R. Srinivasan, Monitoring dynamic thermal behavior of the carbon anode in a lithium-ion cell using a four-probe technique, J. Power Sources 198 (2012) 351–358, http://dx.doi.org/10.1016/j.jpowsour.2011.09.077.

[23] G. Zhu, K. Wen, W. Lv, X. Zhou, Y. Liang, F. Yang, Z. Chen, M. Zou, J. Li, Y. Zhang, W. He, Materials insights into low-temperature performances of lithium-ion batteries, J. Power Sources 300 (2015) 29–40, http://dx.doi.org/10.1016/j.jpowsour.2015.09.056.

[24] X. Wang, X. Wei, Q. Chen, J. Zhu, H. Dai, Lithium-ion battery temperature online estimation based on fast impedance calculation, J. Energy Storage 26 (2019) 100952, http://dx.doi.org/10.1016/j.est.2019.100952.

[25] M. Mathew, S. Janhunen, M. Rashid, F. Long, M. Fowler, Comparative analysis of lithium-ion battery resistance estimation techniques for battery management systems, Energies 11 (6) (2018) 1490, http://dx.doi.org/10.3390/en11061490.

[26] X. Zhang, Q. Wu, X. Guan, F. Cao, C. Li, J. Xu, Lithium dendrite-free and fast-charging for high voltage nickel-rich lithium metal batteries enabled by bi-functional sulfone-containing electrolyte additives, J. Power Sources 452 (2020) 227833, http://dx.doi.org/10.1016/j.jpowsour.2020.227833.

[27] S. Casino, P. Niehoff, M. Börner, M. Winter, Protective coatings on silicon particles and their effect on energy density and specific energy in lithium ion battery cells: A model study, J. Energy Storage 29 (2020) 101376, http://dx.doi.org/10.1016/j.est.2020.101376.

[28] K.H. Kim, J. Shon, H. Jeong, H. Park, S.-J. Lim, J.S. Heo, Improving the cyclability of silicon anodes for lithium-ion batteries using a simple pre-lithiation method, J. Power Sources 459 (2020) 228066, http://dx.doi.org/10.1016/j.jpowsour.2020.228066.

[29] J. Sturm, A. Rheinfeld, I. Zilberman, F.B. Spingler, S. Kosch, F. Frie, A. Jossen, Modeling and simulation of inhomogeneities in a 18650 nickel-rich, silicon-graphite lithium-ion cell during fast charging, J. Power Sources 412 (2019) 204–223, http://dx.doi.org/10.1016/j.jpowsour.2018.11.043.

[30] I. Zilberman, J. Sturm, A. Jossen, Reversible self-discharge and calendar aging of 18650 nickel-rich, silicon-graphite lithium-ion cells, J. Power Sources 425 (2019) 217–226, http://dx.doi.org/10.1016/j.jpowsour.2019.03.109.

[31] I. Zilberman, S. Ludwig, A. Jossen, Cell-to-cell variation of calendar aging and reversible self-discharge in 18650 nickel-rich, silicon–graphite lithium-ion cells, J. Energy Storage 26 (2019) 100900, http://dx.doi.org/10.1016/j.est.2019.100900.

[32] F.M. Kindermann, A. Noel, S.V. Erhard, A. Jossen, Long-term equalization effects in Li-ion batteries due to local state of charge inhomogeneities and their impact on impedance measurements, Electrochim. Acta 185 (2015) 107–116, http://dx.doi.org/10.1016/j.electacta.2015.10.108.

[33] A. Barai, G.H. Chouchelamane, Y. Guo, A. McGordon, P. Jennings, A study on the impact of lithium-ion cell relaxation on electrochemical impedance spectroscopy, J. Power Sources 280 (2015) 74–80, http://dx.doi.org/10.1016/j.jpowsour.2015.01.097.

[34] Q.-A. Huang, Y. Shen, Y. Huang, L. Zhang, J. Zhang, Impedance characteristics and diagnoses of automotive lithium-ion batteries at 7.5% to 93.0% state of charge, Electrochim. Acta 219 (2016) 751–765, http://dx.doi.org/10.1016/j.electacta.2016.09.154.

[35] M. Schönleber, C. Uhlmann, P. Braun, A. Weber, E. Ivers-Tiffée, A consistent derivation of the impedance of a lithium-ion battery electrode and its dependency on the state-of-charge, Electrochim. Acta 243 (2017) 250–259, http://dx.doi.org/10.1016/j.electacta.2017.05.009.

[36] P.J. Osswald, S.V. Erhard, J. Wilhelm, H.E. Hoster, A. Jossen, Simulation and measurement of local potentials of modified commercial cylindrical cells, J. Electrochem. Soc. 162 (10) (2015) A2099–A2105, http://dx.doi.org/10.1149/2.0561510jes.

[37] C. Campestrini, M.F. Horsche, I. Zilberman, T. Heil, T. Zimmermann, A. Jossen, Validation and benchmark methods for battery management system functionalities: State of charge estimation algorithms, J. Energy Storage 7 (2016) 38–51, http://dx.doi.org/10.1016/j.est.2016.05.007.

[38] M. Schmidt, U. Heider, A. Kuehner, R. Oesten, M. Jungnitz, N. Ignat'ev, P. Sartori, Lithium fluoroalkylphosphates: A new class of conducting salts for electrolytes for high energy lithium-ion batteries, J. Power Sources 97–98 (2001) 557–560, http://dx.doi.org/10.1016/S0378-7753(01)00640-1.

[39] R. Amin, Y.-M. Chiang, Characterization of electronic and ionic transport in $li_{1-x}ni_{0.33}mn_{0.33}co_{0.33}o_2$ (nmc_{333}) and $li_{1-x}ni_{0.50}mn_{0.20}co_{0.30}o_2$ (nmc_{523}) as a function of li content, J. Electrochem. Soc. 163 (8) (2016) A1512–A1517, http://dx.doi.org/10.1149/2.0131608jes.

[40] S. Wang, M. Yan, Y. Li, C. Vinado, J. Yang, Separating electronic and ionic conductivity in mix-conducting layered lithium transition-metal oxides, J. Power Sources 393 (2018) 75–82, http://dx.doi.org/10.1016/j.jpowsour.2018.05.005.

[41] S.S. Zhang, K. Xu, T.R. Jow, The low temperature performance of Li-ion batteries, J. Power Sources 115 (1) (2003) 137–140, http://dx.doi.org/10.1016/S0378-7753(02)00618-3.

[42] S. Gantenbein, M. Weiss, E. Ivers-Tiffée, Impedance based time-domain modeling of lithium-ion batteries: Part I, J. Power Sources 379 (2018) 317–327, http://dx.doi.org/10.1016/j.jpowsour.2018.01.043.

[43] A. Jossen, Fundamentals of battery dynamics, J. Power Sources 154 (2) (2006) 530–538, http://dx.doi.org/10.1016/j.jpowsour.2005.10.041.

[44] U. Krewer, F. Röder, E. Harinath, R.D. Braatz, B. Bedürftig, R. Findeisen, Review—Dynamic models of li-ion batteries for diagnosis and operation: A review and perspective, J. Electrochem. Soc. 165 (16) (2018) A3656–A3673, http://dx.doi.org/10.1149/2.1061814jes.

[45] M. Park, X. Zhang, M. Chung, G.B. Less, A.M. Sastry, A review of conduction phenomena in Li-ion batteries, J. Power Sources 195 (24) (2010) 7904–7929, http://dx.doi.org/10.1016/j.jpowsour.2010.06.060.

[46] A. Nyman, T.G. Zavalis, R. Elger, M. Behm, G. Lindbergh, Analysis of the polarization in a li-ion battery cell by numerical simulations, J. Electrochem. Soc. 157 (11) (2010) A1236, http://dx.doi.org/10.1149/1.3486161.

[47] J. Illig, M. Ender, T. Chrobak, J.P. Schmidt, D. Klotz, E. Ivers-Tiffée, Separation of charge transfer and contact resistance in lifepo 4 -cathodes by impedance modeling, J. Electrochem. Soc. 159 (7) (2012) A952–A960, http://dx.doi.org/10.1149/2.030207jes.

[48] R.W. Powell, The thermal and electrical conductivity of carbon and graphite to high temperatures, Proc. Phys. Soc. (1939).

[49] R.A. Buerschaper, Thermal and electrical conductivity of graphite and carbon at low temperatures, J. Appl. Phys. 15 (5) (1944) 452–454, http://dx.doi.org/10.1063/1.1707454.

[50] R.C. Chittick, J.H. Alexander, H.F. Sterling, The preparation and properties of amorphous silicon, J. Electrochem. Soc. 116 (1) (1969) 77, http://dx.doi.org/10.1149/1.2411779.

[51] G. Moumouzias, G. Ritzoulis, D. Siapkas, D. Terzidis, Comparative study of LiBF4, LiAsF6, LiPF6, and LiClO4 as electrolytes in propylene carbonate–diethyl carbonate solutions for Li/LiMn2O4 cells, J. Power Sources 122 (1) (2003) 57–66, http://dx.doi.org/10.1016/S0378-7753(03)00348-3.

[52] W. Waag, S. Käbitz, D.U. Sauer, Experimental investigation of the lithium-ion battery impedance characteristic at various conditions and aging states and its influence on the application, Appl. Energy 102 (2013) 885–897, http://dx.doi.org/10.1016/j.apenergy.2012.09.030.

[53] A. Senyshyn, M.J. Mühlbauer, O. Dolotko, H. Ehrenberg, Low-temperature performance of Li-ion batteries: The behavior of lithiated graphite, J. Power Sources 282 (2015) 235–240, http://dx.doi.org/10.1016/j.jpowsour.2015.02.008.

[54] S.J. An, J. Li, C. Daniel, D. Mohanty, S. Nagpure, D.L. Wood, The state of understanding of the lithium-ion-battery graphite solid electrolyte interphase (SEI) and its relationship to formation cycling, Carbon 105 (2016) 52–76, http://dx.doi.org/10.1016/j.carbon.2016.04.008.

[55] Q. Zhang, Q. Guo, R.E. White, A new kinetic equation for intercalation electrodes, J. Electrochem. Soc. 153 (2) (2006) A301, http://dx.doi.org/10.1149/1.2142287.

[56] C.-K. Huang, J.S. Sakamoto, J. Wolfenstine, S. Surampudi, The limits of low-temperature performance of li-ion cells, J. Electrochem. Soc. 147 (8) (2000) 2893, http://dx.doi.org/10.1149/1.1393622.

[57] C.-M. Wu, C.-C. Chang, M. Avdeev, P.-I. Pan, W.-H. Li, In operando detection of lithium diffusion behaviors at low temperature in 18650 Li-ion battery anode, Physica B 551 (2018) 305–308, http://dx.doi.org/10.1016/j.physb.2018.02.032.

[58] M. Doyle, Modeling of galvanostatic charge and discharge of the lithium/polymer/insertion cell, J. Electrochem. Soc. 140 (6) (1993) 1526, http://dx.doi.org/10.1149/1.2221597.

[59] T.F. Fuller, Simulation and optimization of the dual lithium ion insertion cell, J. Electrochem. Soc. 141 (1) (1994) 1, http://dx.doi.org/10.1149/1.2054684.

[60] A. Barai, K. Uddin, W.D. Widanage, A. McGordon, P. Jennings, A study of the influence of measurement timescale on internal resistance characterisation methodologies for lithium-ion cells, Sci. Rep. 8 (1) (2018) 21, http://dx.doi.org/10.1038/s41598-017-18424-5.

[61] A. Latz, J. Zausch, Thermodynamic derivation of a Butler–Volmer model for intercalation in Li-ion batteries, Electrochim. Acta 110 (2013) 358–362, http://dx.doi.org/10.1016/j.electacta.2013.06.043.

[62] K. Xu, Toward reliable values of electrochemical stability limits for electrolytes, J. Electrochem. Soc. 146 (11) (1999) 4172, http://dx.doi.org/10.1149/1.1392609.

[63] T.F. Fuller, Relaxation phenomena in lithium-ion-insertion cells, J. Electrochem. Soc. 141 (4) (1994) 982, http://dx.doi.org/10.1149/1.2054868.

[64] K.S. Ng, C.-S. Moo, Y.-P. Chen, Y.-C. Hsieh, Enhanced coulomb counting method for estimating state-of-charge and state-of-health of lithium-ion batteries, Appl. Energy 86 (9) (2009) 1506–1511, http://dx.doi.org/10.1016/j.apenergy.2008.11.021.

[65] M. Becherif, M.C. Péra, D. Hissel, S. Jemei, Enhancement of the Coulomb counter estimator by the on-board vehicle determination of battery initial state of charge, IFAC Proc. Vol. 45 (21) (2012) 621–626, http://dx.doi.org/10.3182/20120902-4-FR-2032.00109.

[66] M.A. Awadallah, B. Venkatesh, Accuracy improvement of SOC estimation in lithium-ion batteries, J. Energy Storage 6 (2016) 95–104, http://dx.doi.org/10.1016/j.est.2016.03.003.

[67] Y. Zou, X. Hu, H. Ma, S.E. Li, Combined state of charge and state of health estimation over lithium-ion battery cell cycle lifespan for electric vehicles, J. Power Sources 273 (2015) 793–803, http://dx.doi.org/10.1016/j.jpowsour.2014.09.146.

[68] J. Schmitt, A. Maheshwari, M. Heck, S. Lux, M. Vetter, Impedance change and capacity fade of lithium nickel manganese cobalt oxide-based batteries during calendar aging, J. Power Sources 353 (2017) 183–194, http://dx.doi.org/10.1016/j.jpowsour.2017.03.090.

[69] M.A. Hannan, M. Lipu, A. Hussain, A. Mohamed, A review of lithium-ion battery state of charge estimation and management system in electric vehicle applications: Challenges and recommendations, Renew. Sustain. Energy Rev. 78 (2017) 834–854, http://dx.doi.org/10.1016/j.rser.2017.05.001.

[70] L. Tao, J. Ma, Y. Cheng, A. Noktehdan, J. Chong, C. Lu, A review of stochastic battery models and health management, Renew. Sustain. Energy Rev. 80 (2017) 716–732, http://dx.doi.org/10.1016/j.rser.2017.05.127.